



Full length article

Polystyrene nanoplastics trigger ferroptosis in *Nrf2*-deficient gut via ether phospholipid accumulation

Boxuan Liang ^{a,1}, Xiyun Huang ^{a,1}, Zhiming Li ^{a,1}, Yuji Huang ^{a,b,1}, Yanhong Deng ^a, Xiaoqing Chen ^a, Yizhou Zhong ^{a,b}, Xiaohong Yang ^a, Yu Feng ^a, Ruobing Bai ^a, Bingchi Fan ^a, Hongyi Xian ^a, Hao Li ^a, Shiyue Tang ^a, Zhenlie Huang ^{a,b,*}

^a National Medical Products Administration (NMPA) Key Laboratory for Safety Evaluation of Cosmetics, Guangdong Provincial Key Laboratory of Tropical Disease Research, Department of Toxicology, School of Public Health, Southern Medical University, Guangzhou 510515, China

^b Department of Cardiovascular Surgery, Zhujiang Hospital, Southern Medical University, Guangzhou, China

ARTICLE INFO

Editor: Dr Frederic Coulon

Keywords:

Emerging contaminants
Epithelial-specific *Nrf2* deficiency
Ferroptosis
Lipid metabolism
Ether phospholipid

ABSTRACT

The widespread environmental presence of nanoplastics (NPs) raises significant concerns about their health impacts, particularly on the gastrointestinal system, as NPs are primarily ingested. While previous studies have linked NP-induced intestinal toxicity to oxidative stress and reactive oxygen species (ROS) accumulation, the specific mechanisms of cell death remain unclear. Here, we showed that environmentally relevant concentrations of polystyrene nanoplastics (PS-NPs) induced ferroptosis, a form of lipid peroxidation-driven cell death, in intestinal epithelial cells. Using intestinal epithelial-specific *Nrf2*-deficient mice (*Nrf2*^{f/f}-*Vil*^{Cre+}) and human intestinal epithelial Caco-2 cells, we demonstrated that *Nrf2*, a key oxidative stress regulator, play a protective role against PS-NP-induced ferroptosis. PS-NP exposure disrupted ether phospholipid metabolism, leading to the accumulation of polyunsaturated fatty acid-ether phospholipids and heightened lipid peroxidation in the intestines of *Nrf2*^{f/f}-*Vil*^{Cre+} mice. This accumulation increased the susceptibility of intestinal epithelial cells to ferroptosis. Additionally, a high-fat diet further exacerbated this effect, suggesting that individuals with reduced NRF2 activity and poor dietary habits may be especially vulnerable to PS-NP-induced intestinal damage. Our findings offered new insights into the molecular mechanisms of NP-induced intestinal toxicity and underscored

Abbreviations: PS-NPs, polystyrene nanoplastics; NPs, nanoplastics; MPs, microplastics; ROS, reactive oxygen species; SEM, scanning electron microscopy; DLS, dynamic light scattering; PDI, polydispersity index; H&E, hematoxylin-eosin; TUNEL, terminal deoxynucleotidyl transferase dUTP nick-end labeling; 4-HNE, 4-hydroxynonenal; FC, fold change; PBS, phosphate-buffered saline; PI, propidium iodide; *Nrf2*, nuclear factor, erythroid derived 2, like 2; *Gpx4*, glutathione peroxidase 4; *Gsta1*, glutathione S-transferase, alpha 1; *Gstp1*, glutathione S-transferase, pi 1; *Gss*, glutathione synthetase; qPCR, quantitative polymerase chain reactions; Fer-1, Ferrostatin-1; BIP-V5, Bax inhibitor peptide V5; Lip-1, Liproxstatin-1; LPO, lipid peroxidation; PUFA-ePL, ether phospholipids containing polyunsaturated fatty acid chain; LA-ePL, ether phospholipid containing linoleic acid (LA, C18:2); ARA-ePL, ether phospholipid containing arachidonic acid (ARA, C20:4); EPA-ePL, ether phospholipid containing eicosapentaenoic acid (EPA, C20:5); DHA-ePL, ether phospholipid containing docosahexaenoic acid (DHA, C22:6); GSEA, gene set enrichment analysis; DGKA2, diacylglycerol kinase; GPD1L, glycerol-3-phosphate dehydrogenase 1-like protein; MBOAT7, lysophospholipid acyltransferase 7; PISD, phosphatidylserine decarboxylase proenzyme, mitochondrial; *Enpp2*, ectonucleotide pyrophosphatase/phosphodiesterase 2; *Pla2g7*, phospholipase A2, group VII. FAR1, Fatty acyl-CoA reductase 1; AGPS, alkyldihydroxyacetonephosphate synthase, peroxisomal; GPAM, glycerol-3-phosphate acyltransferase 1; GPAT4, glycerol-3-phosphate acyltransferase 4; PLA2G7, platelet-activating factor acetylhydrolase; PAFAH1B2, platelet-activating factor acetylhydrolase IB subunit alpha2; LPCAT1, lysophosphatidylcholine acyltransferase 1; LPCAT2, lysophosphatidylcholine acyltransferase 2; TMEM189, plasmamylethanolamine desaturase 1; ENPP2, autotaxin; PUFA, polyunsaturated fatty acid; PUFA-CoA, coenzyme A containing polyunsaturated fatty; LPC, lysophosphatidylcholine; LPE, lysophosphatidylethanolamine; DAG, diacylglycerol; PE, phosphatidylethanolamine; PC, phosphatidylcholine; LPE O, plasmamyl lysophosphatidylethanolamine; LPC O, plasmamyl lysophosphatidylcholine; PUFA-PE P, plasmamyl glycerophosphatidylethanolamine containing polyunsaturated fatty; PUFA-PE O, plasmamyl glycerophosphatidylethanolamine containing polyunsaturated fatty; PUFA-PC O, plasmamyl glycerophosphatidylcholine containing polyunsaturated fatty; *Far1*, fatty acyl CoA reductase 1; *Acls4*, acyl-CoA synthetase long-chain family member 4; FDR, false discovery rate; SD, standard deviation; ANOVA, analysis of variance.

* Corresponding author at: Department of Toxicology, School of Public Health, Southern Medical University, 1023-1063 Shatai Nan Road, Guangzhou 510515, China.

E-mail address: huangzhenlie858252@smu.edu.cn (Z. Huang).

¹ These authors contributed equally to this study.

<https://doi.org/10.1016/j.envint.2025.109367>

Received 4 November 2024; Received in revised form 2 March 2025; Accepted 3 March 2025

Available online 6 March 2025

0160-4120/© 2025 The Author(s). Published by Elsevier Ltd. This is an open access article under the CC BY-NC-ND license (<http://creativecommons.org/licenses/by-nd/4.0/>).

the health risks posed by environmental PS-NP exposure, particularly in populations with compromised antioxidant defenses.

1. Introduction

The omnipresence of nanoplastics (NPs) in the environment has raised significant concerns about their potential impact on human health (Eriksen et al. 2014; Geyer et al. 2017). Given that oral ingestion is the primary route of NP exposure, the gastrointestinal tract is particularly vulnerable (Cox et al. 2019), necessitating further investigation. Previous studies have shown that high concentrations of NPs induce oxidative stress and reactive oxygen species (ROS) accumulation in intestinal epithelial cells of mice, ultimately leading to cell death (Liang et al. 2021). In various organisms, NP-induced gut toxicity is primarily driven by excessive ROS (Browne et al. 2013; Gao et al. 2019; Gu et al. 2020). While ROS-mediated cell death can occur through both apoptotic and non-apoptotic pathways, including ferroptosis (Chen et al. 2021; Zheng et al. 2022), the predominant pathway in NP-induced cell death remains unclear, and the underlying mechanisms require further elucidation.

Nuclear factor erythroid 2-related factor 2 (*Nrf2*) is a key transcription factor that regulates cellular defense against oxidative stress and promotes antioxidant functions. Studies have demonstrated the critical role of *Nrf2* in mitigating oxidative damage induced by various external agents, including chemicals, nanoparticles, and PM_{2.5} (Chu et al. 2019b; Liu et al. 2022; Xie et al. 2020). Given this, *Nrf2* likely plays an essential role in countering NP-induced cell death in intestinal epithelial cells, while its inactivation may exacerbate the toxic effects of nanoplastics. Considering the genetic polymorphism of *Nrf2* (Shaheen et al. 2010), which leads to variability in its expression and activity among individuals, a substantial portion of the population may exhibit reduced NRF2 activity and heightened sensitivity to NP exposure. Therefore, it is essential to elucidate how *Nrf2* influences NP-induced cell death and to clarify the mechanisms of nanoplastic toxicity in the absence of *Nrf2*.

Previously, we showed that NP exposure leads to neutral lipid accumulation in mouse plasma at concentrations close to environmental levels (Wang et al. 2023), indicating that lipid metabolism is highly vulnerable to NP disruption. Given the central role of lipid metabolism in both apoptotic and non-apoptotic cell death pathways (Magtanong et al. 2016; Martin-Perez et al. 2022; Pope and Dixon 2023), it likely plays a significant role in NP-induced intestinal toxicity. Notably, *Nrf2* has been implicated in the direct regulation of lipid metabolism, with *Nrf2* deficiency shown to cause lipid accumulation in the liver (Qiu et al. 2022; Shin et al. 2009). We therefore hypothesize that *Nrf2* loss in the gut increases sensitivity to NPs, not only by weakening antioxidant defenses but also by disrupting lipid metabolism, thereby exacerbating NP-induced gut toxicity.

To address this gap, we conducted a 28-day repeated oral exposure experiment in C57BL/6J mice, using polystyrene nanoplastics (PS-NPs) at concentrations ranging from 2.5 mg/kg to 250 mg/kg to determine the threshold for PS-NP-induced intestinal epithelial cell death. These doses encompass both environmentally relevant and hazard identification levels. *In vitro*, we used Annexin V/PI staining to characterize the cell death pathways induced by PS-NPs in the human intestinal epithelial Caco-2 cell model. Using intestinal epithelial-specific *Nrf2* deficiency (*Nrf2*^{fl/fl}-*Vil*^{Cre+}) mice, we explored the critical role of *Nrf2*. Targeted lipidomics was employed to analyze changes in the jejunal lipid profile of *Nrf2*^{fl/fl}-*Vil*^{Cre+} mice following PS-NP exposure, investigating the role of *Nrf2*-mediated lipid metabolism in PS-NP-induced cell death. Additionally, to confirm that *Nrf2* deficiency-related lipid metabolic disruption exacerbates NP-induced gut toxicity, we fed *Nrf2*^{fl/fl}-*Vil*^{Cre+} mice a high-fat diet and assessed gut toxicity under environmentally relevant concentrations of PS-NP exposure. Our findings revealed that PS-NPs induced ferroptosis in *Nrf2*-deficient intestinal epithelial cells

through ether phospholipid accumulation, even at environmentally relevant concentrations.

2. Materials and methods

2.1. Nanoplastics and chemicals

We purchased pristine suspensions of PS-NPs sized at 50 nm from Magsphere (Pasadena, CA, USA). The stock solutions contained a 10 % (w/v) suspension in deionized water, with 0.84 µg/µL sodium azide (NaN₃) as a preservative. The PS-NPs exhibited a density of 1.05 g/cm³, and their detailed characteristics have been previously described (Liang et al. 2024; Liang et al. 2021). All other chemicals were obtained from commercial suppliers, ensuring the highest available purity.

2.2. Particle characterization

We characterized particle sizes morphologically using scanning electron microscopy (SEM) with a Zeiss Supra55 (Carl Zeiss AG, Germany), following established protocols (Liang et al. 2022). Additionally, we assessed the size distribution and zeta potential of the PS-NP suspension in distilled water at a concentration of 0.25 mg/mL using dynamic light scattering (DLS) with a Zetasizer Nano ZS (Malvern Panalytical GmbH, Kassel, Germany).

2.3. Ethical approval

All animal experiments were conducted in accordance with the National Guidelines for Animal Care and Use of China. This study was approved by the Southern Medical University Scientific Research Committee on Ethics in the Care and Use of Laboratory Animals (Permit No. SMUL202308007).

2.4. Generation of mice with intestinal-specific deletion of *Nrf2*

C57BL/6J mice with *Nrf2* alleles flanked by loxP sites were kindly provided by Prof. Jingbo Pi at China Medical University. C57BL/6J mice carrying the *Cre* recombinase gene under the *villin* promoter (*Vil*^{Cre+} mice) were obtained from Gempharmatech Co., Ltd (Jiangsu, China). We bred *Nrf2*^{fl/fl} mice with *Vil*^{Cre+} mice to generate *Nrf2*^{fl/fl}-*Vil*^{Cre+} progeny, which were then backcrossed with *Nrf2*^{fl/fl} mice, resulting in *Nrf2*^{fl/fl}-*Vil*^{Cre+} and *Nrf2*^{fl/fl}-*Vil*^{Cre-} offspring. The *Nrf2*^{fl/fl}-*Vil*^{Cre+} mice exhibited intestinal-specific deletion of *Nrf2*, while *Nrf2*^{fl/fl}-*Vil*^{Cre-} mice served as wild-type controls.

2.5. Mouse husbandry

All mice were housed in a controlled environment with a 12-h light/dark cycle (lights on from 8:00 a.m. to 8:00 p.m.), maintained at 23–25 °C with 50–60 % humidity. They had *ad libitum* access to sterilized water and food throughout the study. At the beginning of the experiments, mice were randomly assigned to groups based on their body weights.

2.6. 28-day repeated dose oral toxicity experiment in mice

We enrolled twenty-four male C57BL/6J mice, eighteen male *Nrf2*^{fl/fl}-*Vil*^{Cre+} mice, and eighteen male *Nrf2*^{fl/fl} mice, each weighing 18–20 g, for the 28-day repeated-dose oral toxicity experiments. The mice received daily oral gavage of either double-distilled water or varying concentrations of pristine PS-NPs dissolved in double-distilled water at a

volume of 10 mL/kg body weight for 28 consecutive days. Body weights were measured weekly between 8:00 and 9:00 a.m., with gavage volumes adjusted accordingly.

2.7. High-fat diet treatment experiment

Twelve *Nrf2*^{fl/fl}-*Vil*^{Cre+} and Twelve *Nrf2*^{fl/fl} male mice, each weighing 18–20 g, were subjected to this experiment. The mice were randomly assigned into three groups based on genotype ($n = 4$ per group). Each group received daily oral gavage of either double-distilled water, 0.25 mg/kg, or 2.5 mg/kg pristine PS-NPs, dissolved in double-distilled water, at a volume of 10 mL/kg body weight for 28 consecutive days. Throughout the exposure period, all mice were provided with a high-fat diet (Western diet, 60 % fat content; Guangdong Medical Laboratory Animal Center).

2.8. Sample collection

At the conclusion of each experiment, the mice were gently anesthetized with 3 % pentobarbital and perfused with ice-cold saline solution to optimize tissue preservation. Following this, cervical dislocation was performed to euthanize the animals humanely. Jejunal tissue samples were promptly collected on ice to maintain their integrity and were subsequently transported frozen to the analytical laboratory, where they were stored at –80 °C until analysis. Additionally, jejunal samples from each experimental group were carefully retrieved post-perfusion and prefixed in 4 % paraformaldehyde. After fixation, these samples were prepared for staining and thorough pathological examination.

2.9. Histopathological analysis

Fixed intestinal tissues ($n = 3$ per group) were dehydrated through a graded series of ethanol, cleared in xylene, and embedded in paraffin wax at 56 °C. Sections were prepared for subsequent staining procedures, including hematoxylin and eosin (H&E) and terminal deoxynucleotidyl transferase dUTP nick-end labeling (TUNEL) staining, and were subsequently examined under an FSX100 microscope (Olympus).

2.10. TUNEL assay

The Click-iT® TUNEL Alexa Fluor® 488 Imaging Assay (Invitrogen) was utilized for *in situ* detection of cell death, following the manufacturer's instructions ($n = 3$ per group). Slides were imaged promptly using consistent settings on an Olympus BX53 fluorescence microscope (Olympus, Japan) or alternatively scanned with the Pannoramic MIDI system (3D HISTECH). The resulting images were subsequently reviewed using Pannoramic Viewer software (3D HISTECH).

2.11. Immunofluorescence

Paraffin-embedded jejunal sections ($n = 3$ per group) were incubated with rabbit anti-4-hydroxynonenal (anti-4-HNE) (1:500; Bioss) and counterstained with DAPI (1 µg/mL; Sigma-Aldrich) for nuclear visualization. Slides were imaged using an Olympus BX53 fluorescence microscope (Olympus, Japan) or scanned with the Pannoramic MIDI system. The images were reviewed using Pannoramic Viewer software. Following our previous study, we quantified fluorescent intensity in each image (Liang et al. 2022). Two independent researchers conducted a blinded analysis of 4-HNE levels, measuring fluorescence area. For each animal, one section was prepared for each target site, with three images acquired per target region for quantification.

2.12. Cell culture and treatment

Caco-2 cells (ATCC® HTB-37™, Manassas, VA, USA) were

maintained in complete Dulbecco's Modified Eagle Medium (DMEM; Gibco, #C11995500BTx), supplemented with 10 % (v/v) fetal bovine serum (FBS; Gibco, #10270106) and 5 % penicillin-streptomycin (Gibco, #15140122). Cells were cultured in a humidified atmosphere containing 5 % CO₂ at 37 °C. Mycoplasma contamination was monitored every three months using a One-Step Quickcolor Mycoplasma Detection Kit (Yise Medical Technology, Shanghai, China, #MD001). For all experiments, Caco-2 cells between passages 10 and 25 were plated and used 21 days post-seeding, after differentiation into enterocytes. The culture medium was replaced every two days to support cell growth and differentiation. Differentiated cells were harvested using 0.05 % trypsin-EDTA and seeded into 6-well plates at a density of 1.5 × 10⁵ cells/mL, with 2 mL of suspension per well.

For experimental treatments, PS-NPs and desired inhibitors were diluted in culture medium to their respective final concentrations. The *Nrf2* inhibitor ML358 (Gibco, #15140122) was applied at 2 µM; ferrostatin-1 (Fer-1; Gibco, #15140122) at 10 µM; liproxstatin-1 (Lip-1; MCE, #950455-15-9) at 200 nM; BIP-V5 (MCE, #579492-81-2) at 20 µM; and Z-VAD-FMK (MCE, #161401-82-7) at 20 µM. Solutions were vortexed thoroughly to ensure uniform dispersion. Before treatment, cell monolayers were washed with pre-warmed phosphate-buffered saline (PBS) to remove residual serum proteins and debris. Treatment suspensions were pre-warmed to 37 °C to align with cell culture conditions. Subsequently, 2 mL of PS-NP suspension, with or without inhibitors, was added to each well and incubated for 24 h under standard culture conditions.

2.13. Protein extraction and western blot

Nuclear protein extracts were prepared using the Nuclear and Cytoplasmic Protein Extraction Kit (Beyotime, China, #P0027) following the manufacturer's protocol. Protein samples were separated by sodium dodecyl sulfate-polyacrylamide gel electrophoresis and transferred onto polyvinylidene fluoride membranes (Bio-Rad Laboratories, CA, USA). Membranes were blocked with 5 % nonfat milk at room temperature for 1 h and incubated overnight at 4 °C with primary antibodies. After three washes with Tris-buffered saline containing 0.1 % Tween-20, membranes were incubated with horseradish peroxidase-conjugated secondary antibodies for 2 h at room temperature. Protein bands were detected using the Western Lightning Plus-ECL detection system (PerkinElmer, Waltham, MA, USA), and band intensities were quantified using ImageJ software. Details of the antibodies used are provided in [Supplementary Table S2](#).

2.14. Lipid peroxide assay

Caco-2 cells ($n = 4$ per group) were seeded into six-well plates and treated with varying concentrations of PS-NPs, the *Nrf2* inhibitor ML358, ferroptosis inhibitors (Fer-1 and Lip-1), and apoptosis inhibitors (BIP-V5 and Z-VAD-FMK) for 2 h. Following treatment, cells were washed three times with PBS before lipid peroxides were quantified using the Liperfluo kit (Dongren Chemical Technology Co., Ltd., Shanghai, China), following the manufacturer's instructions. Cells were stained with a working solution of Liperfluo, prepared by diluting 50 µg of Liperfluo in 60 µL of 1 mmol/L dimethyl sulfoxide, then further diluting to 1 µmol/L with PBS. After a 30-min incubation at 37 °C, the cells were washed three times with PBS and imaged at 20 × magnification using an Olympus BX53 confocal fluorescence microscope.

2.15. Detection of death cells

We assessed various types of cell death using an Annexin V fluorescein isothiocyanate (FITC) Apoptosis Detection Kit I (BD Biosciences, Waltham, MA, USA). Caco-2 cells ($n = 3$ per group) were treated for 24 h with different concentrations of PS-NPs, in combination with the ferroptosis inhibitors (Fer-1 and Lip-1), apoptosis inhibitors (BIP-V5 and Z-

VAD-FMK), and the *Nrf2* inhibitor ML358. Following treatment, cells were collected and washed twice with cold PBS, then resuspended in $1 \times$ binding buffer at a concentration of 1.0×10^6 cells/mL. To each tube, 5 μ L of Annexin V FITC was added to 400 μ L of the cell suspension, and the mixture was incubated at room temperature. After 15 min, 10 μ L of propidium iodide (PI) was added, and the reaction was allowed to proceed for 5 min at 4 °C in the dark. The apoptotic status of the cells was analyzed using flow cytometry (Becton Dickinson, Franklin Lakes, NJ, USA), detecting Annexin V FITC with the FL1 channel and PI with either the FL2 or FL3 channel. Data were analyzed using FlowJo 7.6.1 (Tree Star Inc, Ashland, OR, USA). In this assay, cells were classified as follows: FITC Annexin V (+)/PI (+) were counted as necrotic cells; FITC Annexin V (+)/PI (-) as apoptotic cells; and FITC Annexin V (-)/PI (+) as cells undergoing non-apoptotic cell death.

2.16. Lipidomic sample preparation and lipidome analysis

We conducted lipidomic analysis using six biological samples from each treatment or control group, considering each mouse jejunal tissue as an individual sample. Lipid concentrations were quantified via ultraperformance liquid chromatography (AB Sciex, Toronto, Canada), employing an Agilent Eclipse Plus C18 column (Agilent Technologies) and coupled with an AB Sciex QTRAP 5500 mass spectrometer. Each 20 mg sample of jejunal tissue was spiked with an internal standard mixture (400 pmol each) prior to Folch extraction. Detailed procedures for sample preparation and instrumental determination are provided in the *Supporting Information*. Our quality assurance and control protocols included processing solvent blanks, solvent spiked with internal standards, matrix blanks without internal standards, and commercial jejunal tissue samples as quality control samples to evaluate intra- and interbatch coefficients of variation. Concentrations were calculated by relating the peak areas of the analytes to those of their respective internal standards.

2.17. Label-free proteomics

Label-free proteomics analysis was conducted by Shanghai Applied Protein Technology Co., Ltd. (Shanghai, China). Jejunum tissues were collected from 20 adult mice in each group, with 3 to 4 jejunal samples randomly pooled into each replicate. Three replicates were performed for each group. The label-free quantitative proteomics methods employed have been described in detail previously (Zhong et al. 2022). We quantitatively analyzed pooled samples using label-free mass spectrometry. Liquid chromatography-tandem mass spectrometry data from the mouse jejunum samples were analyzed with MaxQuant (version 1.3.0.5) against the UniprotKB/SwissProt database (2017). Proteins were considered quantifiable if identified at least twice across the three biological replicates. Differentially expressed proteins were identified based on a *P*-value <0.05 and $|\log_2 \text{fold change (FC)}| \geq \log_2 1.2$. Normalization of the protein levels with significant modulation was achieved through division, and the resulting data were analyzed in R (version 4.3.1) using the clusterProfiler package (version 3.14.0) (Yu et al. 2012). Gene set enrichment analysis (GSEA) was meticulously performed utilizing the clusterProfiler package (v. 3.14.0) in R (Yu et al. 2012), applying enrichment criteria of a false discovery rate (FDR) of ≤ 0.1 and a *P*-value of ≤ 0.05 .

2.18. Bulk RNA-seq

Strand-specific libraries from intestinal samples were prepared using the TruSeq Stranded Total RNA Sample Preparation Kit (Illumina, San Diego, CA, USA), following the manufacturer's protocol ($n = 6$ per group). Sequencing read counts were quantified with StringTie (version 1.3.0). Expression levels across different samples were normalized using the trimmed mean of M values method. These normalized expression levels were subsequently converted into fragments per kilobase of

transcript per million mapped reads. Differential gene expression between experimental groups was analyzed, and *P*-values were calculated using the edgeR package (version 3.32.1) in R (McCarthy et al. 2012), followed by adjustments for multiple hypothesis testing. GSEA was performed using the clusterProfiler package (version 3.14.0) in R (Yu et al. 2012), applying enrichment criteria with FDR of ≤ 0.1 and a *P*-value of ≤ 0.05 .

2.19. RNA isolation and quantitative polymerase chain reaction (qPCR)

Frozen animal tissues ($n = 5$ per group) were homogenized in Trizol (Invitrogen, CA, USA), and total RNA was isolated according to the manufacturer's protocol. For qPCR analysis, mRNA cDNA was synthesized using the Evo M–MLV One Step RT-PCR Kit (Accurate Biotechnology, China) following the manufacturer's instructions. Primers for mRNA (Table S1) were designed and synthesized by Tsingke Biotech Co., Ltd. (Beijing, China). qPCR was performed using the SYBR® Green Premix Pro Taq HS qPCR Kit (Accurate Biotechnology) on the ABI QuantStudio™ 6 Flex (Applied Biosystems, USA). The qPCR reaction conditions included an initial denaturation step of 30 s at 95 °C, followed by 40 cycles of 5 s at 95 °C and 36 s at 61 °C. Primer specificity was confirmed through melting curve analysis, which indicated a single product with the appropriate Tm for each primer set. All samples were analyzed in quadruplicate, and relative mRNA expression was normalized to β -actin. Gene expression relative to the control was calculated using the $2^{-\Delta\Delta CT}$ method.

2.20. Statistical analysis

Data are presented as mean \pm standard deviation (SD) unless otherwise specified. Statistical analyses were conducted using SPSS 21.0 (IBM, Armonk, NY, USA). The normality of data distribution and homogeneity of variances were assessed using the Shapiro-Wilk test and Levene's test, respectively. For datasets meeting the assumptions of normality and homogeneity, we employed a Student's *t*-test or analysis of variance (ANOVA) followed by Tukey's multiple comparisons test. For data that did not satisfy these assumptions, the Mann-Whitney *U* test or Kruskal-Wallis *H* test was utilized. A *P*-value of less than 0.05 was considered statistically significant.

3. Results

3.1. PS-NP exposure induced intestinal damage with lipid peroxidation and upregulated *Nrf2* expression

In this study, pristine PS-NPs were selected as representative nanoplastics. SEM confirmed that the PS-NPs were uniformly spherical, with an average diameter of approximately 50 nm (Fig. S1A). DLS analysis revealed narrow size distributions, and the particles remained stable in double-distilled water (Fig. S1B). The high zeta potential further indicated that the PS-NPs were well-dispersed in water.

To elucidate the toxic effects of PS-NPs on the intestinal barrier, we conducted a 28-day repeated-dose oral toxicity study in C57BL/6J male mice, administering 2.5, 25, and 250 mg/kg of 50 nm PS-NPs. H&E staining did not reveal significant tissue damage in the intestines following PS-NP exposure. However, the ratio of villus height to crypt depth decreased in a dose-dependent manner (Fig. 1A and B). The TUNEL assays and 4-HNE immunofluorescence demonstrated that PS-NPs induced dose-dependent cell death and lipid peroxidation in jejunal epithelial cells (Fig. 1A, C and D). However, PS-NP exposure did not increase mRNA levels of the apoptosis marker gene *Caspase3* in the jejunum, indicating that cell death in this tissue is non-apoptotic (Fig. 1E). Given the pivotal role of *Nrf2* in regulating oxidative stress and lipid peroxidation, we performed qPCR to assess the mRNA expression of *Nrf2* and its downstream targets related to lipid peroxidation, including glutathione peroxidase 4 (*Gpx4*), glutathione S-

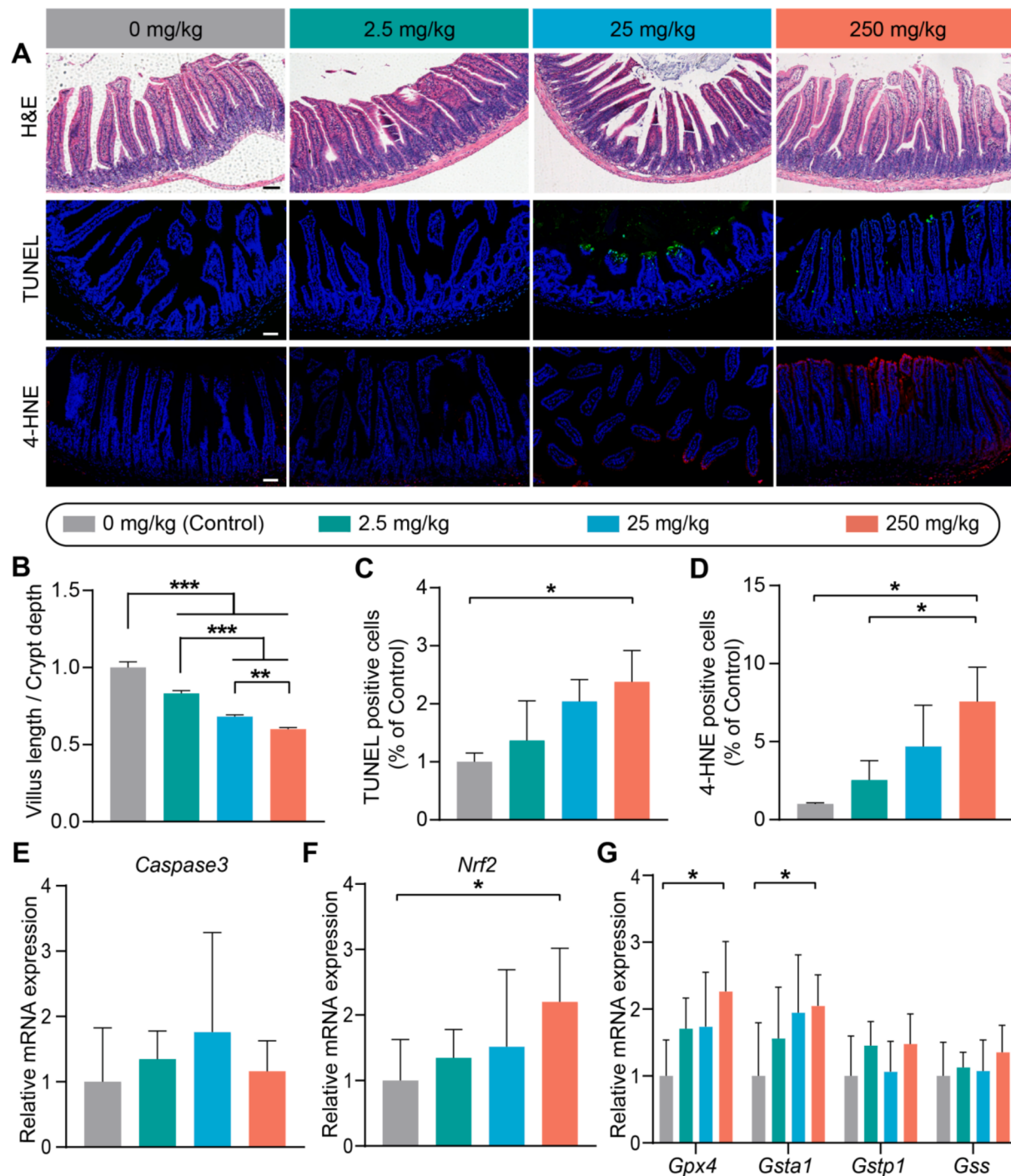


Fig. 1. PS-NP exposure induced jejunal injury in C57BL/6J mice. (A) Representative images of H&E staining, TUNEL assay, and 4-HNE immunofluorescence in the jejunum. Black scale bars represent 100 μ m, and white scale bars represent 50 μ m. (B) Ratio of jejunal villus length to crypt depth. (C) Relative percentages of TUNEL-positive cells. (D) Relative percentages of 4-HNE-positive cells. (E) mRNA expression levels of Caspase3 in the jejunum. (F) mRNA expression levels of Nrf2 in the jejunum. (G) mRNA expression of Gpx4, Gsta1, Gstp1 and Gss in the jejunum. $n = 3$ per group for panels (A-D); $n = 5$ per group for panels (E-G). Statistical analyses were conducted using ANOVA followed by Tukey's method. * $P < 0.05$, ** $P < 0.01$, and *** $P < 0.001$ compared to the control group.

transferase, alpha 1 (*Gsta1*), glutathione S-transferase, pi 1 (*Gstp1*), and glutathione synthetase (*Gss*). The results showed a dose-dependent increase in the mRNA expression of *Nrf2*, *Gpx4*, and *Gsta1* in the jejunum (Fig. 1F and G). Overall, these findings suggest that PS-NPs induced non-apoptotic cell death in mouse intestines, characterized by lipid peroxidation, with *Nrf2* likely playing a key role in this process.

3.2. Ps-nps induced ferroptosis in intestinal epithelial cells with *Nrf2* as an antagonist

To investigate the specific pathways of PS-NP-induced damage to mouse intestines, we conducted *in vitro* experiments using human intestinal epithelial Caco-2 cell lines. A schematic overview of the experiments and parameters assessed is presented in Fig. 2A. Consistent with our previous *in vivo* findings, exposure to PS-NPs resulted in a dose-dependent increase in *NRF2* mRNA expression (Fig. 2B). Furthermore,

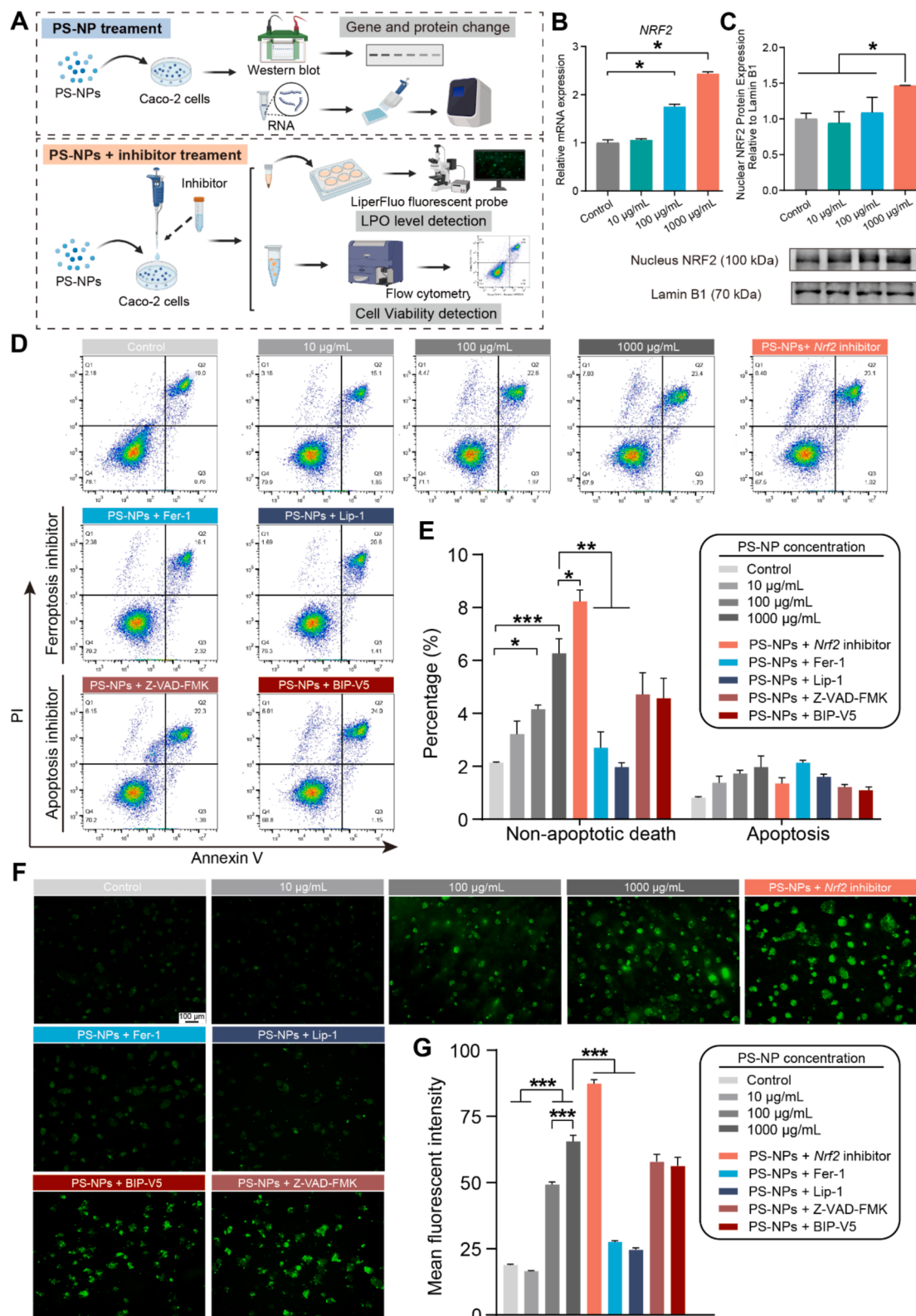


Fig. 2. *Nrf2* antagonized ferroptosis triggered by PS-NPs in intestinal epithelial cells. (A) Schematic overview of the experiments conducted and the parameters assessed in this study. (B) mRNA expression levels of *NRF2* in Caco-2 cells. (C) Protein levels of NRF2 in nucleus. (D) Representative flow cytometry images depicting the frequencies of apoptotic and non-apoptotic cell populations. (E) Percentages of apoptotic and non-apoptotic cells. (F) Representative images of LipoFluo fluorescent probe showing lipid peroxidation fluorescence in Caco-2 cells. (G) Relative lipid peroxidation levels in Caco-2 cells. $n = 3$ per group for panels (B-E); $n = 4$ per group for panels (F, G). In all experimental groups where pretreated with inhibitors, the PS-NPs concentration was 1000 µg/mL. Statistical analyses were performed using ANOVA followed by Tukey's multiple comparison tests. * $P < 0.05$, ** $P < 0.01$, and *** $P < 0.001$ compared to the control group.

PS-NP exposure induced a significant increase in NRF2 nuclear translocation (Fig. 2C). Flow cytometry analysis showed that PS-NPs primarily induced non-apoptotic cell death, with no significant increase in apoptotic cell death in Caco-2 cells (Fig. 2D, E). The rise in non-apoptotic cell death was effectively reversed by pre-treatment with the ferroptosis inhibitors Fer-1 or Lip-1, whereas *Nrf2* inhibition further amplified this effect. In contrast, pre-treatment with the apoptosis inhibitors Z-VAD-FMK and BIP-V5 had no impact on PS-NP-induced cell death (Fig. 2D, E). Moreover, PS-NP exposure resulted in a dose-dependent increase in lipid peroxidation levels, which was effectively reversed by pre-treatment with the ferroptosis inhibitors Fer-1 or Lip-1, while *Nrf2* inhibition significantly exacerbated lipid peroxidation. In

contrast, apoptosis inhibitors had a negligible effect on PS-NP-induced lipid peroxidation (Fig. 2F, G). These findings suggest that PS-NPs induced non-apoptotic cell death, primarily ferroptosis, in intestinal epithelial cells, with *Nrf2* acting as a critical antagonist in this process.

3.3. *Nrf2* deficiency exacerbated PS-NP-induced ferroptosis in intestinal epithelial cells

To investigate the role of *Nrf2* in PS-NP-induced intestinal damage, we employed a mouse model with intestinal epithelial-specific *Nrf2* deficiency (*Nrf2*^{f/f}-*Vil*^{Cre+}) alongside their genotype control (*Nrf2*^{f/f}) mice. We conducted a 28-day repeated-dose oral toxicity study using the

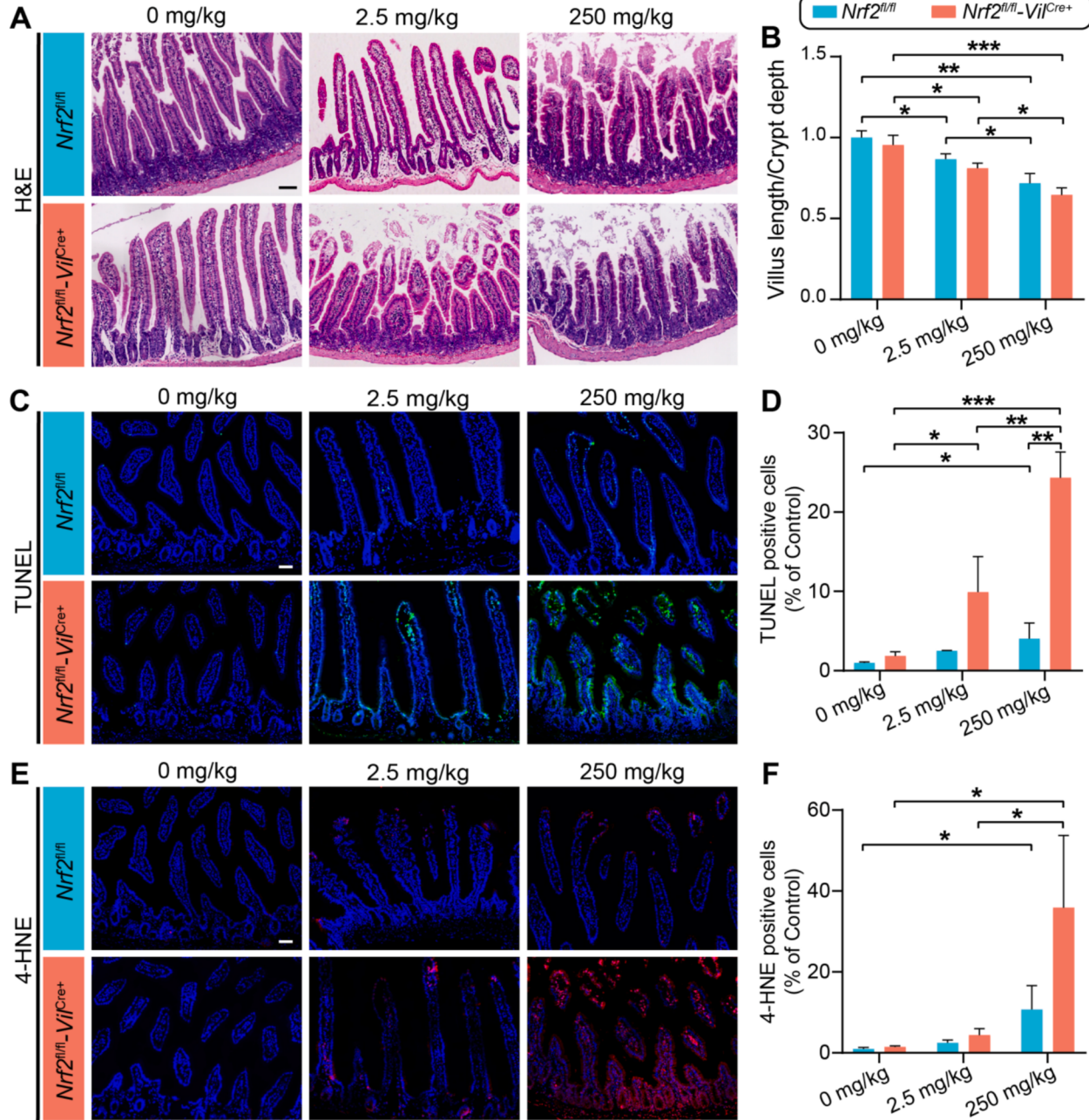


Fig. 3. Intestinal toxicity induced by PS-NPs exposure in *Nrf2*^{f/f}-*Vil*^{Cre+} mice. (A) Representative images of H&E staining in the jejunum. Black scale bars represent 100 μ m. (B) Ratio of jejunal villus length to crypt depth. (C) Representative images from the TUNEL assay in the jejunum. White scale bars represent 50 μ m. (D) Relative percentages of positive staining cells in the TUNEL assay. (E) Representative images of 4-HNE immunofluorescence. White scale bars represent 50 μ m. (F) Relative percentages of positive staining cells for 4-HNE immunofluorescence. $n = 3$ per group for panels (A-F). Statistical analyses were performed using ANOVA followed by Tukey's method. * $P < 0.05$, ** $P < 0.01$, and *** $P < 0.001$ compared to the control group.

same concentration range as in our previous experiments (Huang et al. 2023; Liang et al. 2024; Liang et al. 2022; Liang et al. 2021; Wang et al. 2023). H&E staining after PS-NP exposure did not reveal significant tissue damage in either genotype. However, the ratio of villus height to crypt depth decreased, with a more pronounced reduction observed in *Nrf2*^{fl/fl}-*Vil*^{Cre+} mice (Fig. 3A and B). TUNEL assay indicated that PS-NPs induced more severe cell death in *Nrf2*^{fl/fl}-*Vil*^{Cre+} mice, as evidenced by a higher proportion of intestinal cell death compared to *Nrf2*^{fl/fl} mice at the same exposure concentration, along with significant intestinal cell death at lower exposure doses (2.5 mg/kg) in *Nrf2*^{fl/fl}-*Vil*^{Cre+} mice (Fig. 3C and D). Concurrently, 4-HNE immunofluorescence results showed that PS-NPs induced higher levels of lipid peroxidation in *Nrf2*^{fl/fl}-*Vil*^{Cre+} mice compared to *Nrf2*^{fl/fl} mice (Fig. 3E and F). Collectively, these findings suggest that *Nrf2* deficiency exacerbated ferroptosis induced by PS-NPs in the intestinal epithelium, underscoring the critical role of *Nrf2* in regulating this process.

3.4. *Nrf2* deficiency exacerbated disruption of intestinal lipid metabolism induced by PS-NPs

Given that *Nrf2* deficiency significantly elevated lipid peroxidation under PS-NP exposure, we investigated whether this deficiency also disrupts lipid metabolism beyond merely increasing oxidative stress. Targeted lipidomics analysis revealed significant differences across PS-NP exposures and mouse genotypes, encompassing 1,778 lipids from 34 subclasses (Fig. 4A). Principal component analysis of the lipid profiles indicated clear clustering based on both PS-NP exposure and genotype, suggesting distinct lipidomic alterations in the two mouse genotypes (Fig. 4B). Notably, PS-NP exposure resulted in nearly equal numbers of upregulated and downregulated lipids in *Nrf2*^{fl/fl} mice (56 upregulated, 58 downregulated), whereas in *Nrf2*^{fl/fl}-*Vil*^{Cre+} mice, the majority of altered lipids were upregulated (108 upregulated, 1 downregulated) (Fig. 4C). This finding indicated that *Nrf2* deficiency exacerbated lipid accumulation in jejunal tissue under PS-NP exposure.

Specifically, in *Nrf2*^{fl/fl} mice, lyso-ether phospholipids were the primary lipid species altered by PS-NP exposure (Fig. 4E). In contrast, *Nrf2*^{fl/fl}-*Vil*^{Cre+} mice exhibited significant changes in ether phospholipids (ePLs), including ether phosphatidylethanolamines (ePE) and ether phosphatidylcholines (ePC) (Fig. 4E). Further analysis revealed that lipids enriched in *Nrf2*^{fl/fl} typically contained shorter fatty acyl chains, comprising medium- and long-chain species (12–18 carbons) (Fig. 4D). However, *Nrf2*^{fl/fl}-*Vil*^{Cre+} mice displayed a marked increase in lipid molecules with highly unsaturated acyl tails, including polyunsaturated fatty acids (PUFAs) and very long-chain fatty acids exceeding 20 carbons (Fig. 4D). Additionally, while *Nrf2*^{fl/fl} mice predominantly featured lipids with monounsaturated fatty acids, *Nrf2*^{fl/fl}-*Vil*^{Cre+} mice mainly accumulated lipids with polyunsaturated fatty acids. Lipid abundance analysis demonstrated a significant accumulation of ether phospholipids containing polyunsaturated fatty acid chains (PUFA-ePLs) in the jejunal tissues of *Nrf2*^{fl/fl}-*Vil*^{Cre+} mice following PS-NP exposure (Fig. 4F). Among these PUFA-ePLs, docosahexaenoic acid-ether phospholipids (DHA-ePLs) and arachidonic acid-ether phospholipids (ARA-ePLs) were the most significantly accumulated types (Fig. 4G). Taken together, these findings suggest that *Nrf2* deficiency under PS-NP exposure led to substantial accumulation of PUFA-ePLs, potentially contributing to elevated lipid peroxidation levels and increased sensitivity to ferroptosis in the jejunal tissue of mice.

3.5. Ps-nps induced ferroptosis in *Nrf2*-deficient mice via ether phospholipid accumulation

To further investigate the mechanisms by which PS-NPs disrupt lipid metabolism in the mouse jejunum, we conducted proteomic and transcriptomic analyses. GSEA of the proteomic data revealed significant activation of the glycerophospholipid metabolism pathway in *Nrf2*^{fl/fl}-*Vil*^{Cre+} mice following PS-NP exposure (Fig. 5A–C). This aligns with our

observation that PS-NPs primarily induced phospholipid accumulation in the lipidome.

Given the limitations of proteomic throughput, we extended our investigation to transcriptomic analysis of the jejunum to gain a more comprehensive understanding of the pathways involved in PS-NP-induced lipid metabolic disorders (Fig. 5D and E). Transcriptomic data revealed that, compared to *Nrf2*^{fl/fl} mice, the majority of differentially expressed genes in *Nrf2*^{fl/fl}-*Vil*^{Cre+} mice were upregulated following PS-NP exposure (Fig. 5D). GSEA of transcriptomic data further confirmed the activation of lipid metabolism pathways, particularly those involved in ether phospholipid metabolism (Fig. 5E). These results were subsequently validated by qPCR (Fig. 5F and Fig. S2).

A combined analysis of lipid metabolome, proteome, and transcriptome highlighted alterations in glycerophospholipid and ether phospholipid metabolic profiles (Fig. 5G). Following PS-NP exposure, the ether phospholipid metabolic pathway was activated, with ether phospholipids containing PUFAs, such as plasmanyl glycerophosphatidylethanolamine containing polyunsaturated fatty (PUFA-PE O), plasmanyl glycerophosphatidylethanolamine containing polyunsaturated fatty (PUFA-PE P), and plasmanyl glycerophosphatidylcholine containing polyunsaturated fatty (PUFA-PC O), showing increased expression. Most proteins and genes associated with this pathway exhibited elevated expression levels. Notably, *Nrf2*^{fl/fl}-*Vil*^{Cre+} mice displayed a more pronounced activation of the ether phospholipid metabolism pathway (Fig. 5G).

3.6. *Nrf2* deficiency predisposed high-fat diet-fed mice to PS-NP-induced ferroptosis in intestinal epithelial cells

To confirm that *Nrf2* deficiency exacerbates PS-NP-induced ferroptosis in intestinal epithelial cells by disrupting lipid homeostasis, we conducted a 28-day repeated-dose oral toxicity study under high-fat diet conditions. The study involved exposure to 0.25 and 2.5 mg/kg of 50 nm PS-NPs in both *Nrf2*^{fl/fl} and *Nrf2*^{fl/fl}-*Vil*^{Cre+} mice (Fig. 6A). A schematic summarizing the major metabolic pathways of PUFA-ePLs and key metabolic proteins is provided (Fig. 6B). Lipidomics analysis revealed an increase in PUFA-ePL abundance in jejunal tissue from both genotypes following PS-NP exposure under a high-fat diet. Notably, in *Nrf2*^{fl/fl}-*Vil*^{Cre+} mice exhibited a significant rise in PUFA-ePLs even at the lower PS-NP exposure concentration (0.25 mg/kg). At the same exposure concentration, the increase in PUFA-ePLs was more pronounced in *Nrf2*^{fl/fl}-*Vil*^{Cre+} mice compared to *Nrf2*^{fl/fl} mice (Fig. 6C). H&E staining of the jejunum showed that even at 0.25 mg/kg PS-NPs, the villus height-to-crypt depth ratio was reduced in *Nrf2*^{fl/fl}-*Vil*^{Cre+} mice on a high-fat diet (Fig. 6D and E). The TUNEL assay and 4-HNE immunofluorescence indicated significantly higher levels of cell death and oxidative damage in the jejunal tissue of *Nrf2*^{fl/fl}-*Vil*^{Cre+} mice compared to *Nrf2*^{fl/fl} mice under the same exposure conditions (Fig. 6F–I). Furthermore, mRNA levels of proteins involved in PUFA-ePL metabolism were significantly elevated in the jejunal tissue of *Nrf2*^{fl/fl}-*Vil*^{Cre+} mice on a high-fat diet following PS-NP exposure (Fig. 6J and Fig. S3). Overall, these findings suggest that, under high-fat diet conditions, *Nrf2*^{fl/fl}-*Vil*^{Cre+} mice were more susceptible to PS-NP exposure, resulting in activation of the PUFA-ePL metabolic pathway, increased PUFA-ePL accumulation, and ultimately, intestinal ferroptosis.

4. Discussion

The intestine serves as the primary entry point through which the human body encounters and ingests microplastics (MPs) and NPs, making it a critical target organ for exposure to PS-NPs (Cox et al. 2019). Our previous studies demonstrated that short-term exposure to high concentrations of PS-NPs induces oxidative stress and intestinal damage in mice, with the jejunum exhibiting the most pronounced pathological alterations (Liang et al. 2021). However, the toxicity and underlying molecular mechanisms of long-term exposure to environmentally

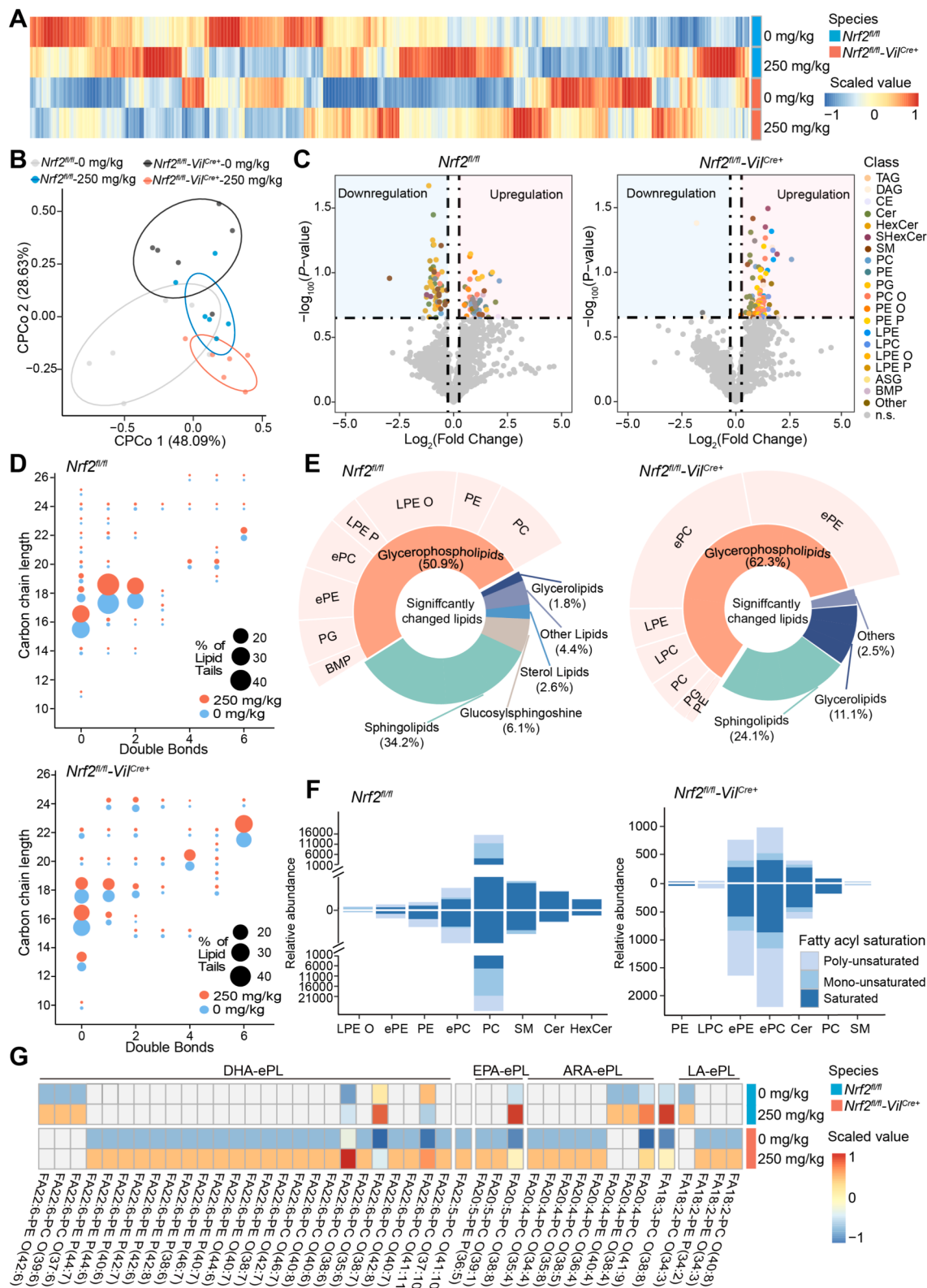


Fig. 4. PS-NPs disrupted lipid metabolism in the jejunum of *Nrf2^{fl/fl}-VilCre+* mice. (A) Lipidomics profiling of jejunal tissue after 28 days of repeated PS-NP exposure in *Nrf2^{fl/fl}-VilCre+* mice. (B) Principal component analysis of lipid molecules in the jejunum, illustrating distinct clustering by genotype and treatment. (C) Volcano plot showing lipid subclass alterations between the two mouse genotypes following PS-NP exposure. (D) Characteristics of significantly altered lipid species, including acyl chain length and degree of unsaturation (number of double bonds). (E) Sunburst chart displaying the distribution and relative proportions of lipid subclasses among differentially expressed lipids. (F) Stacked histogram illustrating the relative abundance of polyunsaturated, monounsaturated, and saturated lipids across lipid subclasses. (G) Heatmap of PUFA-ePLs, highlighting their abundance in different treatment groups. $n = 6$ per group for panels (A-G).

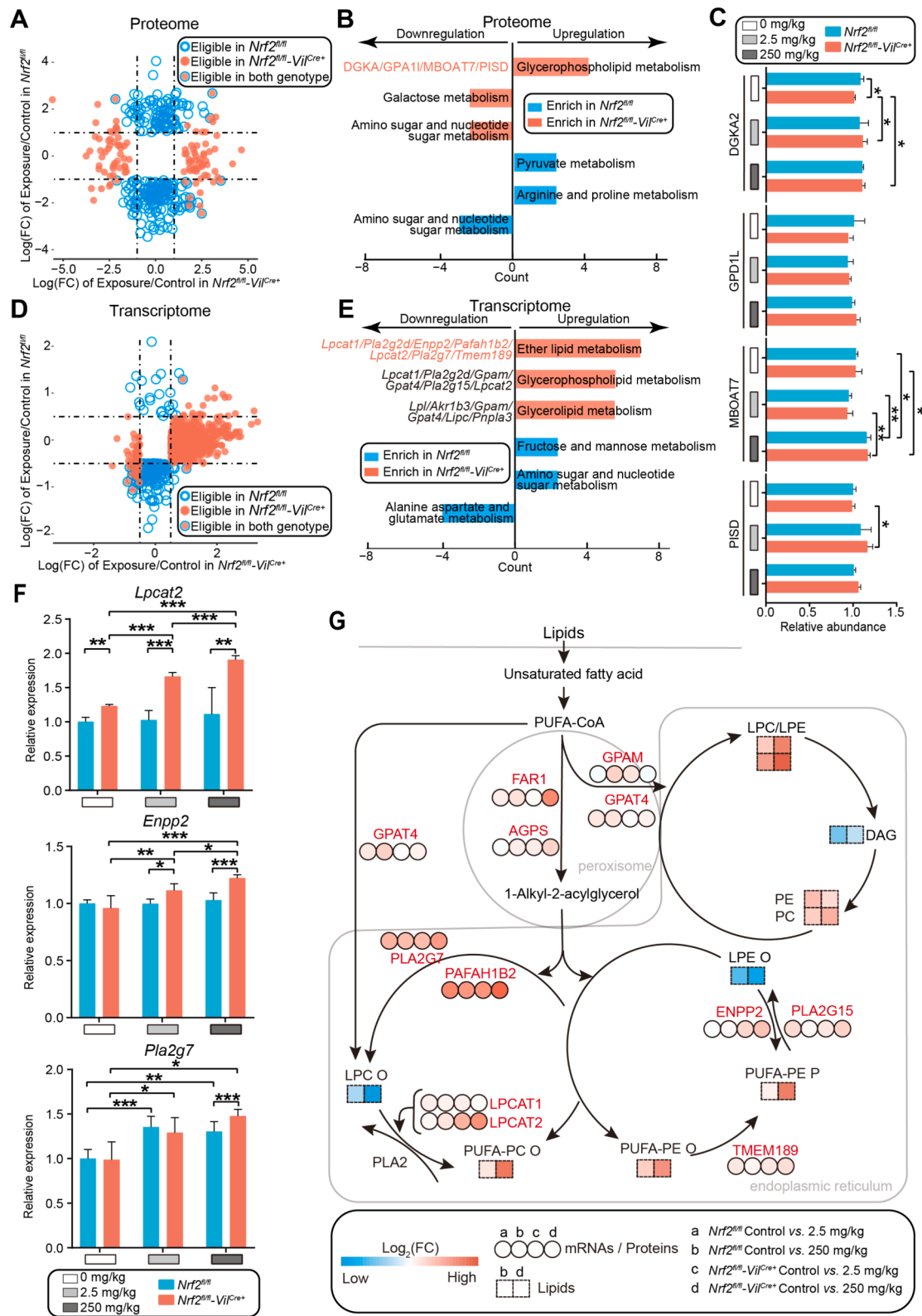


Fig. 5. Nrf2 deficiency exacerbated activation of the ether phospholipid metabolism pathway induced by PS-NPs. (A) Scatter plot comparing the proteome between the control and 250 mg/kg PS-NP groups in both *Nrf2^{fl/fl}* and *Nrf2^{fl/fl}-Vil^{Cre+}* mice. (B) GSEA of differentially expressed proteins in *Nrf2^{fl/fl}* and *Nrf2^{fl/fl}-Vil^{Cre+}* mice. (C) Protein levels involved in the phospholipid metabolism pathway across the 0, 2.5, and 250 mg/kg PS-NP groups. (D) Scatter plot comparing the transcriptome between the control and 250 mg/kg PS-NP groups in both *Nrf2^{fl/fl}* and *Nrf2^{fl/fl}-Vil^{Cre+}* mice. (E) GSEA of differentially expressed genes in *Nrf2^{fl/fl}* and *Nrf2^{fl/fl}-Vil^{Cre+}* mice. (F) qPCR validation of mRNA expression for genes involved in the phospholipid metabolism pathway. (G) Schematic illustration of glycerophospholipid and ether phospholipid metabolic profiles based on lipid metabolome, proteome, and transcriptome data. $n = 3$ per group for panels (A-C); $n = 6$ per group for panels (D, E); $n = 5$ per group for panel F. Statistical analyses were performed using ANOVA followed by Tukey's multiple comparison test. * $P < 0.05$, ** $P < 0.01$, and *** $P < 0.001$ compared to the control group.

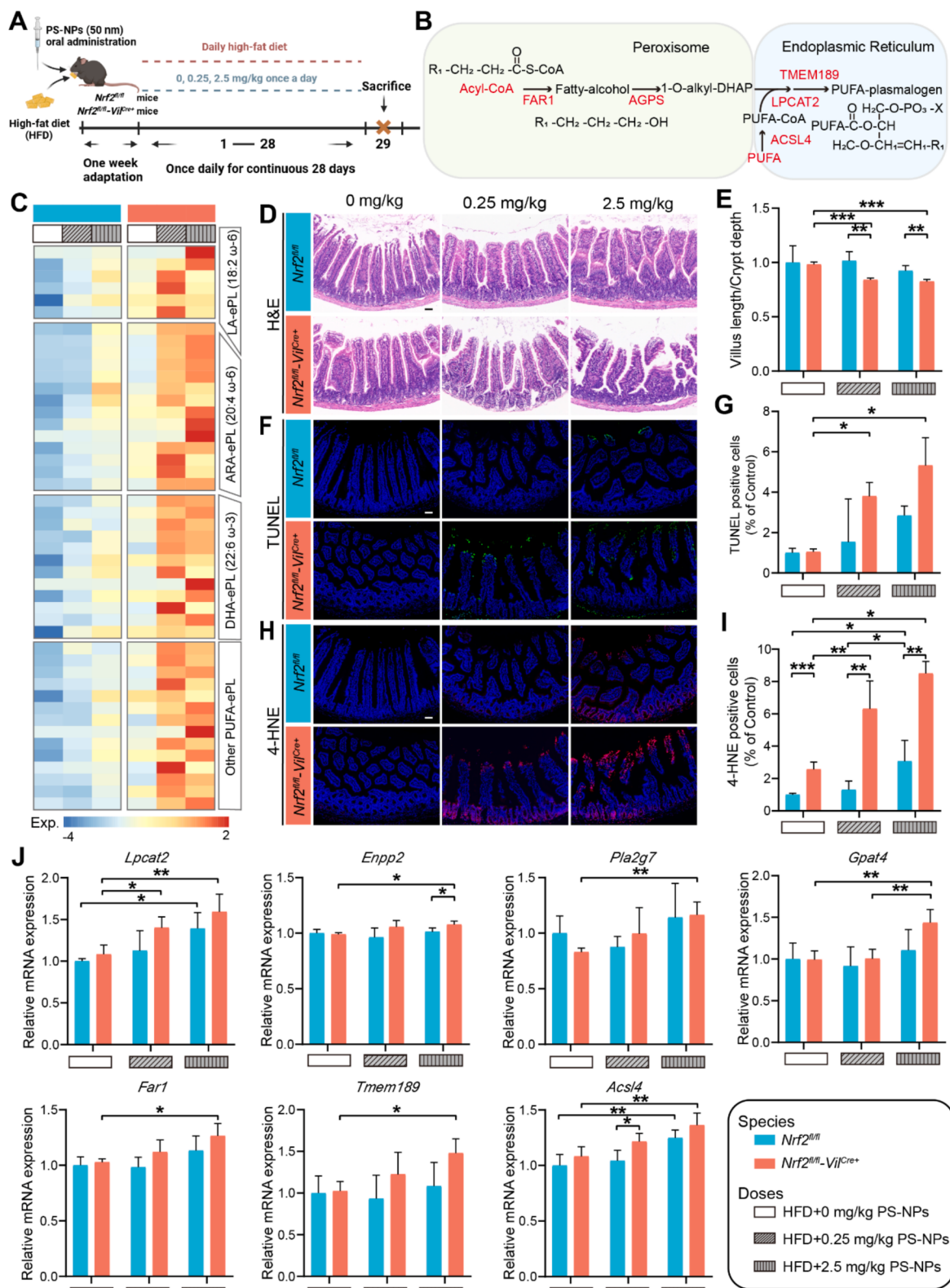


Fig. 6. Intestinal toxicity induced by PS-NPs exposure in *Nrf2*^{fl/fl}-*Vil*^{Cre/+} mice under a high-fat diet. (A) Schematic of the treatment strategy and experimental design. (B) Genes involved in the biosynthesis of PUFA-ePLs. (C) Heatmap showing the abundance of ether phospholipids containing polyunsaturated fatty acid chains across treatment groups. (D) Representative images of H&E staining in the jejunum. Scale bars: 50 μ m (black). (E) Ratio of jejunal villus height to crypt depth. (F) Representative images of TUNEL assay in the jejunum. Scale bars: 50 μ m (white). (G) Relative percentages of TUNEL-positive cells. (H) Representative images of 4-HNE immunofluorescence. (I) Relative percentages of 4-HNE-positive cells. (J) Validation of mRNA expression for genes involved in PUFA-ePL biosynthesis by qPCR. $n = 3$ per group for panels C; $n = 4$ per group for panels (D-J). Statistical analyses were performed using ANOVA followed by Tukey's post-hoc test; * $P < 0.05$, ** $P < 0.01$, and *** $P < 0.001$ compared with the control group.

relevant concentrations of PS-NPs in the intestine remain largely unexplored. To address this gap, we utilized intestine-specific *Nrf2* knockout mice and *in vitro* intestinal epithelial cell models to investigate the toxic effects and potential molecular mechanisms of PS-NPs at environmentally relevant concentrations. Our findings revealed that ferroptosis was the predominant form of cell death induced by PS-NPs, with *Nrf2* playing a crucial protective role. In the absence of *Nrf2*, PS-NP exposure led to significant accumulation of PUFA-ePLs in the mouse intestine, resulting in increased lipid peroxidation and heightened sensitivity to ferroptosis in the jejunal tissue. Moreover, under high-fat diet conditions, even exposure to environmentally relevant concentrations of PS-NPs significantly increased the susceptibility of intestinal tissue to ferroptosis via this pathway. Our study not only shed light on the molecular mechanisms underlying PS-NP-induced toxicity in intestinal epithelial cells but also highlighted the potential health risks posed by PS-NPs to human intestinal health, particularly in individuals with reduced NRF2 activity and poor dietary habits.

The most significant finding of this study was that PS-NPs primarily induced intestinal damage by triggering ferroptosis in intestinal epithelial cells, particularly under conditions of *Nrf2* deficiency. Although NaN_3 was present in the PS-NP stock solution, its concentration at the highest exposure level in cell experiments was only 0.13 mM, far below the 10 mM threshold known to affect Caco-2 cell viability (Zhou et al. 2005). Moreover, no evidence has been reported linking NaN_3 to ferroptosis, minimizing the potential for confounding effects. Notably, PS-NPs can induce ferroptosis even at environmentally relevant concentrations. Ferroptosis, a form of programmed cell death closely linked to ROS, is characterized by the extensive accumulation of lipid ROS within cells (Chen et al. 2021) and is commonly observed in intestinal epithelial cells during the progression of intestinal diseases (Deng et al. 2021; Xu et al. 2021; Zhou et al. 2020). PS-NPs may exert their toxic effects through two primary mechanisms: inducing oxidative stress and triggering ferroptosis (He et al. 2024), while also compromising membrane integrity (Fleury and Baulin 2021), and further exacerbating ferroptosis. This dual mechanism represents a key pathway through which exogenous substances contribute to intestinal damage (Deng et al. 2021; Xu et al. 2021; Zhou et al. 2020). *Nrf2* is a key transcription factor that regulates cellular responses to oxidative stress, providing essential antioxidant protection. It plays a critical role in defending against oxidative damage induced by exogenous chemicals, nanoparticles, PM2.5, and other environmental stressors (Chu et al. 2019b; Hayes and Dinkova-Kostova 2014; Liu et al. 2022; Xie et al. 2020). Our results found that, in the absence of *Nrf2*, ROS accumulation was exacerbated in the intestine, amplifying the toxic effects of PS-NPs on intestinal epithelial cells. These findings underscored the pivotal role of *Nrf2* in mediating PS-NP-induced ferroptosis in intestinal epithelial cells.

Lipids are key regulators of ferroptosis, with the initiation and execution of this cell death process intricately linked to lipid metabolism (Chu et al. 2019a; Doll et al. 2017; Kagan et al. 2017; Magtanong et al. 2019; Yang et al. 2016; Zou et al. 2019). PS-NPs have been shown to alter lipid metabolism in various organisms, including marine invertebrates, fish, and mice (Deng et al. 2022; Jiang and Zhang 2021; Lai et al. 2021; Yang et al. 2020). At environmentally relevant exposure levels, PS-NPs also lead to the accumulation of neutral lipids in the plasma of mice (Wang et al. 2023). Another major finding of our study was that, beyond its role in mitigating oxidative stress, *Nrf2* deficiency exacerbated PS-NP-induced disruption of lipid metabolism and ferroptosis in intestinal epithelial cells by disturbing lipid homeostasis. The role of *Nrf2* in lipid regulation is pleiotropic and context-dependent (Cuadrado et al. 2019). For instance, *Nrf2* activation is often associated with the repression of lipogenic gene expression (Asantewaa et al. 2024; Kay et al. 2011). In this study, we found that *Nrf2* deficiency led to significant accumulation of PUFA-ether phospholipids in the intestinal tissues of mice exposed to PS-NPs. Ether lipid homeostasis is critical for cellular function, with ether phospholipids containing PUFA at the sn-2

position known to enhance cellular sensitivity to ferroptosis (Cui et al. 2021; Zou et al. 2020). In conclusion, our research demonstrated that the combined effects of PS-NP exposure and *Nrf2* deficiency activated the ether phospholipid metabolism pathway in intestinal epithelial cells, leading to PUFA-ether phospholipid accumulation and increased susceptibility to ferroptosis.

Changes in circulating lipid levels induced by a high-fat diet create a microenvironment conducive to lipid metabolism reprogramming and remodeling (Astudillo et al. 2023; Martin-Perez et al. 2022). Interestingly, when we increased lipid intake in *Nrf2*^{fl/fl}-*Vil*^{Cre+} mice through a high-fat diet, we observed a further increase in their sensitivity to PS-NPs-induced ferroptosis in the intestines. This finding underscored the notion that *Nrf2* deficiency exacerbated PS-NP-induced ferroptosis in intestinal epithelial cells by promoting lipid accumulation. Given the genetic variability of *Nrf2* (Shaheen et al. 2010), individuals with reduced NRF2 activity may be particularly vulnerable to the intestinal toxicity of nanoplastics. Moreover, a significant portion of the population consumes a high-fat diet (Wang et al. 2020), which often includes meat, seafood, and beverages packaged in single-use plastics—items likely to contain substantial MPs (Sun and Wang 2023). This suggests that individuals on high-fat diets may be at heightened risk of MP exposure. Our findings emphasized the need to consider how genetic factors, coupled with unhealthy lifestyle choices, may aggravate the toxicity of NPs.

Based on data suggesting that humans ingest approximately 0.1–5.0 g of MPs weekly (equivalent to roughly 0.2–10 mg/kg body weight/day for a 70 kg adult) (Senathirajah et al. 2021), we employed doses of 2.5 and 25 mg/kg PS-NPs to simulate current environmental human exposure, and 250 mg/kg to assess potential harm. However, the lack of kinetic data on PS-NPs in this study limits the ability to adequately assess the risk of intestinal damage on a hazard basis. Additionally, we included a lower dose of 0.25 mg/kg to examine the combined effects of PS-NPs and a high-fat diet on intestinal toxicity in *Nrf2*^{fl/fl}-*Vil*^{Cre+} mice. It is important to note that this study focused on populations with low intestinal NRF2 activity, as modeled by the *Nrf2*^{fl/fl}-*Vil*^{Cre+} mice, and caution should be exercised when extrapolating these findings to the general population.

The inherently conflicting goals of strict variable control to investigate toxicity mechanisms and simulating real-world conditions to address practical issues necessitate compromises in experimental design. With a focus on exploring the toxicity mechanisms of NPs, we selected pristine 50 nm PS-NPs for this study, consistent with the particle size and material used in our earlier studies (Huang et al. 2023; Liang et al. 2024; Liang et al. 2022; Liang et al. 2021; Wang et al. 2023). This approach allows us to isolate the toxicity of the particles themselves and build upon prior findings for comparative and integrative insights. Nevertheless, polystyrene constitutes only a fraction of environmental MPs and NPs, and variations in polymer types, surface chemistry, and morphologies may result in distinct bioactivities (Xu et al. 2020). Although our previous research demonstrated that smaller PS particles exhibit stronger intestinal toxicity, making 50 nm particles particularly relevant for investigating health effects (Liang et al. 2021), it remains unclear whether the mechanisms identified for nanoscale particles apply to larger MPs. Additionally, environmental MPs and NPs often undergo degradation, altering their physicochemical properties and potentially modifying their toxicity. Further research is needed to assess these complexities.

Our findings, derived from transcriptomic, proteomic, and lipidomic analyses, identified ether phospholipids as the most significantly affected lipids in PS-NP-exposed *Nrf2*^{fl/fl}-*Vil*^{Cre+} mice. Moreover, our results indicated that lipid accumulation associated with a high-fat diet markedly exacerbated PS-NP-induced intestinal toxicity in mice, as evidenced by the heightened sensitivity of high-fat diet-fed animals, which exhibited significant intestinal toxicity at lower exposure levels than those on a normal diet. While our results strongly suggest that PUFA-ePLs may mediate PS-NP-induced ferroptosis in intestinal

epithelial cells, we have yet to provide direct causal evidence for this relationship, nor can we exclude the potential contributions of other lipid species. Additional studies are required to validate these findings and fully elucidate the mechanisms involved in lipid-mediated toxicity.

5. Conclusion

Our findings indicated that ferroptosis was the primary form of cell death induced by PS-NPs in intestinal epithelial cells, highlighting the critical protective role of *Nrf2* in this process. In the context of *Nrf2* deficiency, PS-NP exposure caused lipid metabolic dysregulation, leading to the accumulation of lipids, most likely dominated by PUFA-ether phospholipids, and ultimately heightened the sensitivity of intestinal epithelial cells to ferroptosis. Additionally, our results suggest that at environmentally relevant concentrations of PS-NPs, poor dietary habits may heighten the risk of intestinal damage in individuals with low NRF2 activity. This study provides new insights into the role of PS in intestinal diseases and contributes to understanding the growing risk of gastrointestinal disorders associated with PS-NP exposure in humans.

CRediT authorship contribution statement

Boxuan Liang: Writing – original draft, Visualization, Methodology, Formal analysis, Data curation, Conceptualization. **Xiyun Huang:** Writing – original draft, Visualization, Methodology, Formal analysis, Data curation, Conceptualization. **Zhiming Li:** Writing – original draft, Visualization, Methodology, Formal analysis, Data curation, Conceptualization. **Yuji Huang:** Writing – original draft, Visualization, Methodology, Formal analysis, Data curation, Conceptualization. **Yanhong Deng:** Validation, Investigation. **Xiaoqing Chen:** Validation, Investigation. **Yizhou Zhong:** Validation, Investigation. **Xiaohong Yang:** Validation, Investigation. **Yu Feng:** Validation, Investigation. **Ruobing Bai:** Validation, Investigation. **Bingchi Fan:** Validation, Investigation. **Hongyi Xian:** Validation, Investigation. **Hao Li:** Validation, Investigation. **Shiyue Tang:** Visualization. **Zhenlie Huang:** Writing – review & editing, Resources, Project administration, Funding acquisition, Conceptualization.

Declaration of competing interest

The authors declare that they have no known competing financial interests or personal relationships that could have appeared to influence the work reported in this paper.

Acknowledgments

We extend our gratitude to Prof. Jingbo Pi from China Medical University for generously providing the C57BL/6J mice carrying *Nrf2* alleles flanked by loxP sites. This work was supported by grants from the National Natural Science Foundation of China (Grant No. 82473661, 82273656, 82304177, 82073519, 81872601), the Science and Technology Project of Guangdong Province, China (Grant No. 2022A0505050035), the Guangdong Basic Applied Basic Research Foundation (Grant No. 2022A1515010610, Guangdong-Dongguan Joint grant No. 2022A1515111098, Guangdong-Guangzhou Joint grant No. 2023A1515110373), the Chinese Postdoctoral Science Foundation (Grant No. 2023M741553, 2023T160295, 2022M721486), the Postdoctoral Fellowship Program of CPSF (Grant No. GZC20231055, GZC20240653), Dongguan Social Development Science and Technology Project-High Level Hospital Construction Project (Grant No. 20231800905372), the Guangdong Provincial Key Laboratory of Tropical Disease Research (Grant No. 2017B030314035), the National Medical Products Administration (NMPA) Key Laboratory for Safety Evaluation of Cosmetics and the Guangdong Medical Products Administration (GDMPA) Project of Scientific and Technological Innovation (Grant No. 2024ZDZ09), Shenzhen Medical Research Fund (Grant No.

A2402045).

Appendix A. Supplementary data

Supplementary data to this article can be found online at <https://doi.org/10.1016/j.envint.2025.109367>.

Data availability

Data will be made available on request.

References

- Asantewaa, G., Tuttle, E.T., Ward, N.P., Kang, Y.P., Kim, Y., Kavanagh, M.E., Girnius, N., Chen, Y., Rodriguez, K., Hecht, F., Zocchi, M., Smorodintsev-Schiller, L., Scales, T.Q., Taylor, K., Alimohammadi, F., Duncan, R.P., Sechrist, Z.R., Agostini-Vulaj, D., Schafer, X.L., Chang, H., Smith, Z.R., O'Connor, T.N., Whelan, S., Selfors, L.M., Crowdus, J., Gray, G.K., Bronson, R.T., Brenner, D., Rufini, A., Dirksen, R.T., Hezel, A.F., Huber, A.R., Munger, J., Cravatt, B.F., Vasilicou, V., Cole, C.L., DeNicola, G.M., Harris, I.S., 2024. Glutathione synthesis in the mouse liver supports lipid abundance through NRF2 repression. *Nat. Commun.* 15, 6152.
- Astudillo, A.M., Balboa, M.A., Balsinde, J., 2023. Compartmentalized regulation of lipid signaling in oxidative stress and inflammation: plasmalogens, oxidized lipids and ferroptosis as new paradigms of bioactive lipid research. *Prog. Lipid Res.* 89, 101207.
- Browne, M.A., Niven, S.J., Galloway, T.S., Rowland, S.J., Thompson, R.C., 2013. Microplastic moves pollutants and additives to worms, reducing functions linked to health and biodiversity. *Curr. Biol.* 23, 2388–2392.
- Chen, X., Li, J., Kang, R., Klionsky, D.J., Tang, D., 2021. Ferroptosis: machinery and regulation. *Autophagy* 17, 2054–2081.
- Chu, B., Kon, N., Chen, D., Li, T., Liu, T., Jiang, L., Song, S., Tavana, O., Gu, W., 2019a. ALOX12 is required for p53-mediated tumour suppression through a distinct ferroptosis pathway. *Nat. Cell Biol.* 21, 579–591.
- Chu, C., Zhang, H., Cui, S., Han, B., Zhou, L., Zhang, N., Su, X., Niu, Y., Chen, W., Chen, R., Zhang, R., Zheng, Y., 2019b. Ambient PM2.5 caused depressive-like responses through NRF2/NLRP3 signaling pathway modulating inflammation. *J. Hazard. Mater.* 369, 180–190.
- Cox, K.D., Coverton, G.A., Davies, H.L., Dower, J.F., Juanes, F., Dudas, S.E., 2019. Human consumption of microplastics. *Environ. Sci. Tech.* 53, 7068–7074.
- Cuadrado, A., Rojo, A.I., Wells, G., Hayes, J.D., Cousin, S.P., Rumsey, W.L., Attucks, O.C., Franklin, S., Levonen, A.L., Kensler, T.W., Dinkova-Kostova, A.T., 2019. Therapeutic targeting of the NRF2 and KEAP1 partnership in chronic diseases. *Nat. Rev. Drug Discov.* 18, 295–317.
- Cui, W., Liu, D., Gu, W., Chu, B., 2021. Peroxisome-driven ether-linked phospholipids biosynthesis is essential for ferroptosis. *Cell Death Differ.* 28, 2536–2551.
- Deng, S., Wu, D., Li, L., Li, J., Xu, Y., 2021. TBHQ attenuates ferroptosis against 5-fluorouracil-induced intestinal epithelial cell injury and intestinal mucositis via activation of NRF2. *Cell. Mol. Biol. Lett.* 26, 48.
- Deng, Y., Chen, H., Huang, Y., Zhang, Y., Ren, H., Fang, M., Wang, Q., Chen, W., Hale, R. C., Galloway, T.S., Chen, D., 2022. Long-term exposure to environmentally relevant doses of large polystyrene microplastics disturbs lipid homeostasis via bowel function interference. *Environ. Sci. Tech.* 56, 15805–15817.
- Doll, S., Proneth, B., Tyurina, Y.Y., Panzilius, E., Kobayashi, S., Ingold, I., Irmler, M., Beckers, J., Aichler, M., Walch, A., Prokisch, H., Trumbach, D., Mao, G., Qu, F., Bayir, H., Fullekrug, J., Scheel, C.H., Wurst, W., Schick, J.A., Kagan, V.E., Angel, J. P., Conrad, M., 2017. ACSL4 dictates ferroptosis sensitivity by shaping cellular lipid composition. *Nat. Chem. Biol.* 13, 91–98.
- Ericksen, M., Lebreton, L.C., Carson, H.S., Thiel, M., Moore, C.J., Borerro, J.C., Galgani, F., Ryan, P.G., Reisser, J., 2014. Plastic pollution in the world's oceans: more than 5 trillion plastic pieces weighing over 250,000 tons afloat at sea. *PLoS One* 9, e111913.
- Fleury, J.B., Baulin, V.A., 2021. Microplastics destabilize lipid membranes by mechanical stretching. *PNAS* 118.
- Gao, T., Wang, Z., Dong, Y., Cao, J., Lin, R., Wang, X., Yu, Z., Chen, Y., 2019. Role of melatonin in sleep deprivation-induced intestinal barrier dysfunction in mice. *J. Pineal Res.* 67, e12574.
- Geyer, R., Jambeck, J.R., Law, K.L., 2017. Production, use, and fate of all plastics ever made. *Sci. Adv.* 3, e1700782.
- Gu, W., Liu, S., Chen, L., Liu, Y., Gu, C., Ren, H.Q., Wu, B., 2020. Single-cell RNA sequencing reveals size-dependent effects of polystyrene microplastics on immune and secretory cell populations from zebrafish intestines. *Environ. Sci. Tech.* 54, 3417–3427.
- Hayes, J.D., Dinkova-Kostova, A.T., 2014. The Nrf2 regulatory network provides an interface between redox and intermediary metabolism. *Trends Biochem. Sci.* 39, 199–218.
- He, Y., Yu, T., Li, H., Sun, Q., Chen, M., Lin, Y., Dai, J., Wang, W., Li, Q., Ju, S., 2024. Polystyrene nanoplastic exposure activates ferroptosis by oxidative stress-induced lipid peroxidation in porcine oocytes during maturation. *J. Anim. Sci. Biotechnol.* 15, 117.
- Huang, Y., Liang, B., Li, Z., Zhong, Y., Wang, B., Zhang, B., Du, J., Ye, R., Xian, H., Min, W., Yan, X., Deng, Y., Feng, Y., Bai, R., Fan, B., Yang, X., Huang, Z., 2023. Polystyrene nanoplastic exposure induces excessive mitophagy by activating AMPK/

- ULK1 pathway in differentiated SH-SY5Y cells and dopaminergic neurons *in vivo*. Part. Fibre Toxicol. 20, 44.
- Jiang, Q., Zhang, W., 2021. Gradual effects of gradient concentrations of polystyrene nanoplastics on metabolic processes of the razor clams. Environ. Pollut. 287, 117631.
- Kagan, V.E., Mao, G., Qu, F., Angeli, J.P., Doll, S., Croix, C.S., Dar, H.H., Liu, B., Tyurin, V.A., Ritov, V.B., Kapralov, A.A., Amoscato, A.A., Jiang, J., Anthonymuthu, T., Mohammadyani, D., Yang, Q., Proneth, B., Klein-Seetharaman, J., Watkins, S., Bahar, I., Greenberger, J., Mallampalli, R.K., Stockwell, B.R., Tyurina, Y.Y., Conrad, M., Bayir, H., 2017. Oxidized arachidonic and adrenic PEs navigate cells to ferroptosis. Nat. Chem. Biol. 13, 81–90.
- Kay, H.Y., Kim, W.D., Hwang, S.J., Choi, H.S., Gilroy, R.K., Wan, Y.J., Kim, S.G., 2011. Nrf2 inhibits LX α lpha-dependent hepatic lipogenesis by competing with FXR for acetylase binding. Antioxid. Redox Signal. 15, 2135–2146.
- Lai, W., Xu, D., Li, J., Wang, Z., Ding, Y., Wang, X., Li, X., Xu, N., Mai, K., Ai, Q., 2021. Dietary polystyrene nanoplastics exposure alters liver lipid metabolism and muscle nutritional quality in carnivorous marine fish large yellow croaker (*Larimichthys crocea*). J. Hazard. Mater. 419, 126454.
- Liang, B., Deng, Y., Huang, Y., Zhong, Y., Li, Z., Du, J., Ye, R., Feng, Y., Bai, R., Fan, B., Chen, X., Huang, X., Yang, X., Xian, H., Yang, X., Huang, Z., 2024. Fragile guts make fragile brains: intestinal epithelial Nrf2 deficiency exacerbates neurotoxicity induced by polystyrene nanoplastics. ACS Nano 18, 24044–24059.
- Liang, B., Huang, Y., Zhong, Y., Li, Z., Ye, R., Wang, B., Zhang, B., Meng, H., Lin, X., Du, J., Hu, M., Wu, Q., Sui, H., Yang, X., Huang, Z., 2022. Brain single-nucleus transcriptomics highlights that polystyrene nanoplastics potentially induce Parkinson's disease-like neurodegeneration by causing energy metabolism disorders in mice. J. Hazard. Mater. 430, 128459.
- Liang, B., Zhong, Y., Huang, Y., Lin, X., Liu, J., Lin, L., Hu, M., Jiang, J., Dai, M., Wang, B., Zhang, B., Meng, H., Lelaka, J.J.J., Sui, H., Yang, X., Huang, Z., 2021. Underestimated health risks: polystyrene micro- and nanoplastics jointly induce intestinal barrier dysfunction by ROS-mediated epithelial cell apoptosis. Part. Fibre Toxicol. 18, 20.
- Liu, N., Liang, Y., Wei, T., Zou, L., Huang, X., Kong, L., Tang, M., Zhang, T., 2022. The role of ferroptosis mediated by NRF2/ERK-regulated ferritinophagy in CdTe QDs-induced inflammation in macrophage. J. Hazard. Mater. 436, 129043.
- Magtanong, L., Ko, P.J., Dixon, S.J., 2016. Emerging roles for lipids in non-apoptotic cell death. Cell Death Differ. 23, 1099–1109.
- Magtanong, L., Ko, P.J., To, M., Cao, J.Y., Forcina, G.C., Tarangelo, A., Ward, C.C., Cho, K., Patti, G.J., Nomura, D.K., Olzmann, J.A., Dixon, S.J., 2019. Exogenous monounsaturated fatty acids promote a ferroptosis-resistant cell state. Cell Chem. Biol. 26 (420–432), e429.
- Martin-Perez, M., Urdiroz-Urricelqui, U., Bigas, C., Benitah, S.A., 2022. The role of lipids in cancer progression and metastasis. Cell Metab. 34, 1675–1699.
- McCarthy, D.J., Chen, Y., Smyth, G.K., 2012. Differential expression analysis of multifactor RNA-Seq experiments with respect to biological variation. Nucleic Acids Res. 40, 4288–4297.
- Pope, L.E., Dixon, S.J., 2023. Regulation of ferroptosis by lipid metabolism. Trends Cell Biol. 33, 1077–1087.
- Qiu, S., Liang, Z., Wu, Q., Wang, M., Yang, M., Chen, C., Zheng, H., Zhu, Z., Li, L., Yang, G., 2022. Hepatic lipid accumulation induced by a high-fat diet is regulated by Nrf2 through multiple pathways. FASEB J. 36, e22280.
- Senathirajah, K., Attwood, S., Bhagwat, G., Carbery, M., Wilson, S., Palanisami, T., 2021. Estimation of the mass of nanoplastics ingested - A pivotal first step towards human health risk assessment. J. Hazard. Mater. 404, 124004.
- Shaheen, S.O., Newson, R.B., Ring, S.M., Rose-Zerilli, M.J., Holloway, J.W., Henderson, A.J., 2010. Prenatal and infant acetaminophen exposure, antioxidant gene polymorphisms, and childhood asthma. J. Allergy Clin. Immunol. 126 (1141–1148), e1147.
- Shin, S., Wakabayashi, J., Yates, M.S., Wakabayashi, N., Dolan, P.M., Aja, S., Liby, K.T., Sporn, M.B., Yamamoto, M., Kensler, T.W., 2009. Role of Nrf2 in prevention of high-fat diet-induced obesity by synthetic triterpenoid CDDO-imidazolidine. Eur. J. Pharmacol. 620, 138–144.
- Sun, A., Wang, W.-X., 2023. Human exposure to nanoplastics and its associated health risks. Environ. & Health Perspect. 139–149.
- Wang, B., Liang, B., Huang, Y., Li, Z., Zhang, B., Du, J., Ye, R., Xian, H., Deng, Y., Xiu, J., Yang, X., Ichihara, S., Ichihara, G., Zhong, Y., Huang, Z., 2023. Long-chain acyl carnitines aggravate polystyrene nanoplastics-induced atherosclerosis by upregulating MARCO. Adv. Sci. (Weinh.), e2205876.
- Wang, L., Wang, H., Zhang, B., Popkin, B.M., Du, S., 2020. Elevated fat intake increases body weight and the risk of overweight and obesity among Chinese adults: 1991–2015 trends. Nutrients 12.
- Xie, C., Ge, M., Jin, J., Xu, H., Mao, L., Geng, S., Wu, J., Zhu, J., Li, X., Zhong, C., 2020. Mechanism investigation on Bisphenol S-induced oxidative stress and inflammation in murine RAW264.7 cells: The role of NLRP3 inflammasome, TLR4, Nrf2 and MAPK. J. Hazard. Mater. 394, 122549.
- Xu, C., Zhang, B., Gu, C., Shen, C., Yin, S., Aamir, M., Li, F., 2020. Are we underestimating the sources of microplastic pollution in terrestrial environment? J. Hazard. Mater. 400, 123228.
- Xu, S., He, Y., Lin, L., Chen, P., Chen, M., Zhang, S., 2021. The emerging role of ferroptosis in intestinal disease. Cell Death Dis. 12, 289.
- Yang, W.S., Kim, K.J., Gaschler, M.M., Patel, M., Shchepinov, M.S., Stockwell, B.R., 2016. Peroxidation of polyunsaturated fatty acids by lipoxygenases drives ferroptosis. PNAS 113, E4966–E4975.
- Yang, Y., Shao, H., Wu, Q., Wang, D., 2020. Lipid metabolic response to polystyrene particles in nematode *caenorhabditis elegans*. Environ. Pollut. 256, 113439.
- Yu, G., Wang, L.G., Han, Y., He, Q.Y., 2012. clusterProfiler: an R package for comparing biological themes among gene clusters. OMICS 16, 284–287.
- Zheng, D., Liu, J., Piao, H., Zhu, Z., Wei, R., Liu, K., 2022. ROS-triggered endothelial cell death mechanisms: focus on pyroptosis, parthanatos, and ferroptosis. Front. Immunol. 13, 1039241.
- Zhong, Y., Liang, B., Meng, H., Ye, R., Li, Z., Du, J., Wang, B., Zhang, B., Huang, Y., Lin, X., Hu, M., Rong, W., Wu, Q., Yang, X., Huang, Z., 2022. 1,2-Dichloroethane induces cortex demyelination by depressing myelin basic protein via inhibiting aquaporin 4 in mice. Ecotoxicol. Environ. Saf. 231, 113180.
- Zhou, S., Li, Y., Kestell, P., Schafer, P., Chan, E., Paxton, J.W., 2005. Transport of thalidomide by the human intestinal caco-2 monolayers. Eur. J. Drug Metab. Pharmacokinet. 30, 49–61.
- Zhou, Y., Ye, T.J., DeCaro, E., Buehler, B., Stahl, Z., Bonavita, G., Daniels, M., You, M., 2020. Intestinal SIRT1 deficiency protects mice from ethanol-induced liver injury by mitigating ferroptosis. Am. J. Pathol. 190, 82–92.
- Zou, Y., Henry, W.S., Ricq, E.L., Graham, E.T., Phadnis, V.V., Maretich, P., Paradkar, S., Boehnke, N., Deik, A.A., Reinhardt, F., Eaton, J.K., Ferguson, B., Wang, W., Fairman, J., Keys, H.R., Dancik, V., Clish, C.B., Clemons, P.A., Hammond, P.T., Boyer, L.A., Weinberg, R.A., Schreiber, S.L., 2020. Plasticity of ether lipids promotes ferroptosis susceptibility and evasion. Nature 585, 603–608.
- Zou, Y., Palte, M.J., Deik, A.A., Li, H., Eaton, J.K., Wang, W., Tseng, Y.Y., Deasy, R., Kost-Alimova, M., Dancik, V., Leshchiner, E.S., Viswanathan, V.S., Signoretti, S., Choueiri, T.K., Boehm, J.S., Wagner, B.K., Doench, J.G., Clish, C.B., Clemons, P.A., Schreiber, S.L., 2019. A GPX4-dependent cancer cell state underlies the clear-cell morphology and confers sensitivity to ferroptosis. Nat. Commun. 10, 1617.